

Dual-Domain Homogeneous Fusion with Cross-Modal Mamba and Progressive Decoder for 3D Object Detection

Xuzhong Hu, Zaipeng Duan, Pei An, Jun zhang, and Jie Ma

Abstract—Fusing LiDAR point cloud features and image features in a homogeneous BEV space has been widely adopted for 3D object detection in autonomous driving. However, such methods are limited by the excessive compression of multi-modal features. While some works explore feature fusion in dense voxel spaces, they suffer from high computational costs and inefficiencies in query generation. To address these limitations, we propose a Dual-Domain Homogeneous Fusion network (DDHFusion), which leverages the complementary advantages of both BEV and voxel domains while mitigating their respective drawbacks. Specifically, we first transform image features into BEV and sparse voxel spaces using LSS and our proposed semantic-aware feature sampling module which can significantly reduce computational overhead by filtering unimportant voxels. For feature encoding, we design two networks for BEV and voxel feature fusion, incorporating novel cross-modal voxel and BEV Mamba blocks to resolve feature misalignment and enable efficient yet comprehensive scene perception. The output voxel features are injected into the BEV space to compensate for the loss of 3D details caused by height compression. In addition, a progressive query generation module is implemented in the BEV domain to alleviate false negatives during query selection caused by feature compression and small object sizes. Finally, a progressive decoder can sequentially aggregate not only context-rich BEV features but also geometry-aware voxel features, ensuring more precise confidence prediction and bounding box regression. On the NuScenes dataset, DDHFusion achieves state-of-the-art performance, and further experiments demonstrate its superiority over other homogeneous fusion methods.

Index Terms—3D object detection, autonomous driving, multi-modal, homogeneous fusion, Mamba.

I. INTRODUCTION

AUTONOMOUS driving has emerged as a highly active research field, advancing rapidly with the integration of deep learning models. Among its critical technologies, 3D object detection plays a pivotal role in enabling safe and efficient driving planning. In current autonomous systems, LiDAR and cameras serve as essential sensors for environmental perception. LiDAR utilizes laser echo technology to capture precise 3D environmental information in the form of point clouds, while cameras generate images rich in texture information by capturing visible light. By harnessing the complementary strengths of LiDAR and cameras, fusion-based object detectors have consistently outperformed their single-sensor counterparts in terms of accuracy and robustness. However, multi-sensor feature fusion is non-trivial due to the inherent heterogeneity between camera and LiDAR data. Many existing works [1]–[6] attempt to enrich raw point clouds or voxels with image features. However, this approach suffers from semantic

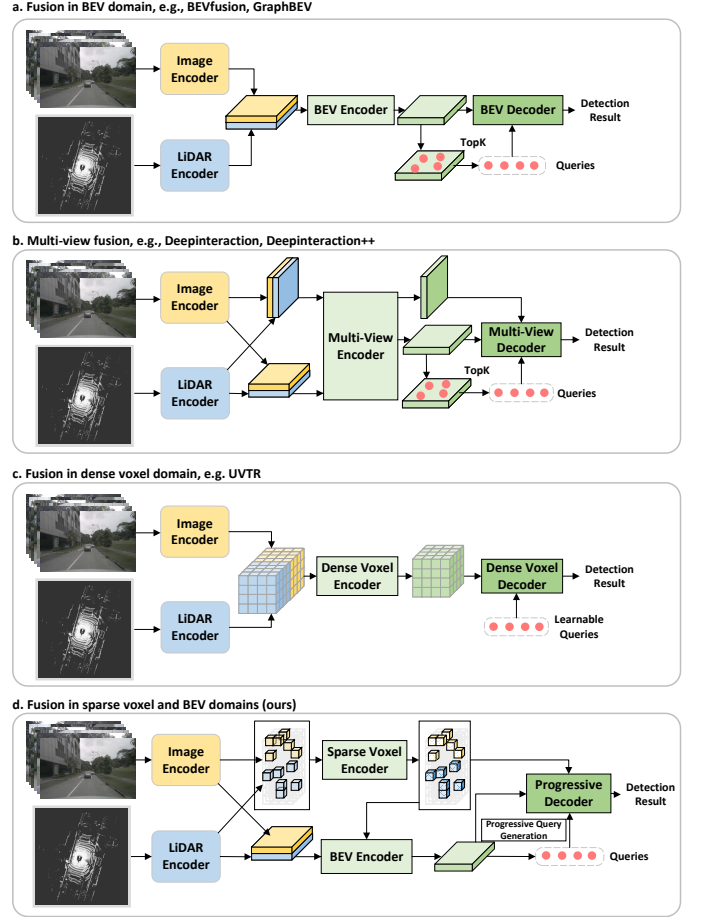


Fig. 1. Overview of homogeneous fusion methods. The view transformation in Fig. 1(a) and Fig. 1(b) causes the loss of modality details. The dense voxel representation in Fig. 1(c) causes computational burden. Our method in Fig. 1(d) combines the advantages of sparse voxel and BEV domains.

information loss during camera-to-LiDAR projection, as only a small fraction of image features are preserved, leading to degraded detection performance in regions with fewer points. Recent studies propose homogeneous fusion strategies [7]–[12] that actively transform image features into a shared representation space with LiDAR features. These methods leverage symmetric network architectures to fully exploit multi-modal complementarity while mitigating performance degradation caused by single-sensor failures.

A popular method [7]–[9], as depicted in Fig. 1(a), employs Lift-Splat-Shoot (LSS) to project image features onto a unified BEV plane for concatenation with LiDAR features. This approach is highly efficient as mature techniques from 2D

detection tasks can be easily adopted for BEV feature fusion and query generation. For the latter, the sample center-based label assignment and Top-K selection strategies are widely applied. However, it also has two limitations: **1) Information Compression:** The compression of geometric and texture information along the height dimension results in blurred BEV features, which further leads to missed detections and reduced regression accuracy. As shown in Fig. 1(b), some works [10], [11] introduce multi-view encoder-decoder structures to address this. However, the additional transformation of LiDAR features back to the frontal view significantly disrupts 3D spatial relationships, still incurring semantic ambiguity. **2) Feature Misalignment:** Inaccurate depth estimation in LSS or calibration errors between sensors may lead to spatial misalignment of multi-modal BEV features. Extra alignment techniques are required before feeding the features into the BEV backbone.

As shown in Fig. 1(c), fusion in a unified voxel space has been explored to retain 3D geometric details and leverage higher-dimensional feature interactions for enhanced spatial perception while avoiding information compression. While theoretically superior to BEV-based fusion, this paradigm faces several challenges: **1) Computational Burden:** Fusing features represented as dense voxels is highly memory-intensive and computationally expensive, making it difficult to deploy in large-scale driving scenarios. **2) Query Generation Difficulty:** According to [13], compared to the BEV domain, the more severe foreground-background imbalance and higher dimensionality in the voxel domain complicate label assignment and input-dependent query generation [14]. [12] adopts randomly initialized 3D learnable queries combined with local 3D deformable attention in decoders, which slows down training convergence and limits the model’s ability to localize potential instances. **3) Feature Misalignment:** The feature misalignment issue becomes even more challenging in the voxel domain. Computational constraints force these methods to rely on 3D convolutions for local feature fusion within limited receptive fields, which hinders feature alignment over larger regions.

In this work, we propose a novel detection framework—the Dual-Domain Homogeneous Fusion network (DDHFusion), which overcomes the limitations of both BEV and voxel fusion domains while leveraging their respective strengths. As shown in Fig. 1(d), the BEV domain is responsible for query generation, while the voxel domain provides geometry-aware features. For clarity, the proposed method is divided into three steps: **1) Feature Transformation:** First, we transform image features into sparse voxel and BEV spaces using the semantic-aware feature sampling (SAFS) and LSS modules. Compared to [12], the sparse voxel representation significantly reduces computational overhead. **2) Feature Encoding:** During encoding, these multi-representation image features interact with LiDAR ones through homogeneous voxel and BEV fusion (HVF and HBF) networks. Within these networks, we introduce cross-modal voxel and BEV mamba blocks (CV-Mamba and CB-Mamba) to resolve feature misalignment and enable efficient global scene perception. **3) Feature Decoding:** For decoding, we propose a progressive query generation (PQG)

module and a progressive decoder (PD). The former activates BEV features with high-response queries, generating potential hard queries in the second stage to mitigate false negatives caused by feature compression and small object sizes. The latter enhances the conventional BEV decoder by integrating fine-grained 3D structural features around targets with our proposed multi-modal voxel feature mixing (MMVFM) module.

As a summary, the main contributions are as follows:

- 1) We introduce DDHFusion for 3D object detection that achieves state-of-the-art performance on the NuScenes dataset, outperforming other homogeneous fusion approaches while maintaining efficient inference.
- 2) To the best of our knowledge, we are the first to extend Mamba into multi-modal 3D detection. The proposed CV-Mamba and CB-Mamba blocks effectively facilitate feature fusion across global voxel or BEV domains.
- 3) We propose the PQG and PQ modules for feature decoding. The former generates easy and difficult queries in stages to minimize false negatives, while the latter adaptively integrates dual-domain features to enhance the accuracy of each query’s regression.

II. RELATED WORK

In this section, we overview homogeneous fusion methods in the BEV and voxel domains, followed by recent advancements in state space models.

A. Homogeneous Fusion in BEV Domain

Fusion in a shared BEV space is a prominent approach for 3D object detection in autonomous driving. A critical step in this process is the transformation of image features into the BEV space. Early work [15] proposed an auto-calibration method: image features are projected onto predefined dense 3D voxel centers, adjusted by regressing offsets, and assigned to corresponding voxels. These features are then compressed along the height dimension to generate BEV features. Building on this, [16] introduced range attention to refine the distribution of intermediate voxel features along the range dimension. Recently, LSS [17] has become widely adopted for view transformation. It projects features into a 3D frustum based on depth estimation and then onto the BEV plane with pooling operation. However, inaccuracies in depth estimation often lead to misalignment between LiDAR and image BEV views. To address this, [18] leverages contrastive learning for feature alignment, while [19] and [20] utilize semantic-guided optical flow estimation or mutual deformable attention for explicit alignment. Additionally, [21] and [20] enhance depth estimation accuracy through edge-aware LiDAR depth maps or local alignment operations.

Unlike the local fusion operations in the aforementioned methods, our approach establishes global relationships both within and across modalities, enabling effective feature alignment and more comprehensive scene perception.

B. Homogeneous Fusion in Voxel Domain

Compared to BEV homogeneous fusion, transforming image features into the voxel domain and fusing them with

LiDAR voxels avoids the information loss caused by height compression. Additionally, introducing multi-modal voxel features during the decoding process leads to better regression accuracy. [22] and [23] unproject image features from each pixel onto virtual points with depth completion and then convert them into voxels, applying voxel pooling to fuse fine-grained multi-modal features. [24] generates virtual points using nearest neighbor matching around the 2D instance mask on the image. [25] improves this approach with k-nearest neighbor matching and introduces gated modality-aware convolution to fuse semantic and geometric features of both camera and LiDAR at different granularities. While these virtual-point-based methods largely address the sparsity issue of LiDAR point clouds, they require additional depth completion or high-resolution instance segmentation networks. It leads to significant training costs, and the labels required for these tasks are often difficult to obtain. In contrast, [12] bypasses the need for extra networks by adopting an LSS-like algorithm. It first assigns image features to predefined dense voxels and then weights them with category-based depth maps. [26] eliminates the depth-weighting step and introduces additional gating mechanisms to enable flexible fusion. However, dense voxel representations incur significant computational overhead. In recent work, [27] only utilize element-wise fusion in the intermediate voxel space during LSS, with subsequent feature propagation occurring in the BEV domain.

In our work, we adopt sparse voxel representation to conserve computational resources. Additionally, our Mamba-based network, HVF, facilitates multi-granularity global feature fusion.

C. State Space Model

State Space Models (SSMs) [28]–[30] describe dynamic systems by representing the system’s internal state at each moment. With advancements in deep learning, SSMs have been integrated into neural networks to achieve more efficient and flexible inference. [31] effectively captures long-term dependencies in sequences by introducing higher-order polynomial projection operators, compressing historical information into a low-dimensional state space. S4 [28], a structured state space model based on [29], enhances computational efficiency and modeling capacity through structured state transition matrices. Building on S4, [32] introduces input-specific state transition mechanisms, significantly boosting both expressiveness and efficiency. Due to its linear complexity, Mamba has been widely adopted in computer vision. For instance, [33] unfolds images into 1D sequences and proposes a bidirectional Mamba module for comprehensive feature learning. [34] extends this approach to four-directional scanning, uncovering richer spatial relationships in images and providing a theoretical analysis of Mamba’s linear attention. Mamba has also been applied to 3D tasks such as point cloud classification [35], 3D object detection [36]–[38], and semantic completion [39]. For example, [36] employs a group-free voxel Mamba module to expand the receptive field across the entire scene, while [39] integrates local adaptive reordering into the Mamba module to enhance local information extraction.

Different from these single-modality architectures for 3D tasks, we extend Mamba to multi-modal ones, further unlocking its potential.

III. METHOD

The pipeline of DDHFusion is shown in Fig. 2. First, multi-view images and LiDAR point clouds are passed through their respective networks for feature extraction. These features are then transformed into sparse voxels V_I, V_L and BEV representations B_I, B_L . Then, two homogeneous fusion networks are introduced to perform feature fusion within their respective domains. The outputs V_I' and V_L' are passed into the BEV fusion network after sparse height compression [40]. After processing through the BEV backbone, the resulting BEV features are used for progressive query generation. These queries are then input into the progressive decoder including both BEV and voxel decoders for classification and box regression. In this section, we provide a detailed introduction to DDHFusion from the following aspects: semantic-aware feature sampling, voxel homogeneous network, BEV homogeneous network, progressive query generation, and progressive decoder.

A. Semantic-Aware Feature Sampling

Describing the entire driving scene using dense voxels is highly redundant. First, a significant portion of voxels corresponds to empty space, where no objects are present. Second, in autonomous driving scenarios, foreground objects typically occupy only a small fraction of the overall scene. This redundancy not only consumes substantial computational resources but also diverts the model’s information extraction capacity to large, irrelevant areas, thereby hindering feature learning.

Drawing inspiration from [41], we propose the SAFS module depicted in Fig. 3 to selectively generate important image voxels. First, the image features F_I from the image backbone are passed through a convolution block to generate the depth map. Similar to LSS, these depths are represented by discrete bins. Another branch predicts the semantic segmentation mask. During training, we project points within ground truth boxes onto the image plane to generate segmentation labels for sparse supervision.

We divide the entire 3D space into voxels V_c with number $H_I \times W_I \times Z_I$. According to [12], we set the height range Z_I twice as that of LiDAR voxels Z_L to obtain more texture details from images. Then, we project voxel centers onto the image plane and collect depth scores V_d and semantic score V_s using bilinear interpolation. The voxels with both scores above certain thresholds are selected:

$$V_c = \{v_{ci} \mid (v_{si} > s) \wedge (v_{di} > d)\} \\ v_{ci} \in V_c, v_{di} \in V_d, v_{si} \in V_s, i \in [0, H_I W_I Z_I - 1] \} \quad (1)$$

At the beginning of training or in some crowd scenarios, the number of V_c' may be too large. Therefore, we set an upper limit N , and if the number exceeds it, the farthest point sampling is applied to retain only N voxels. Finally, we assign image features to V_c' and multiply them by the corresponding depth scores to obtain voxel features V_I .

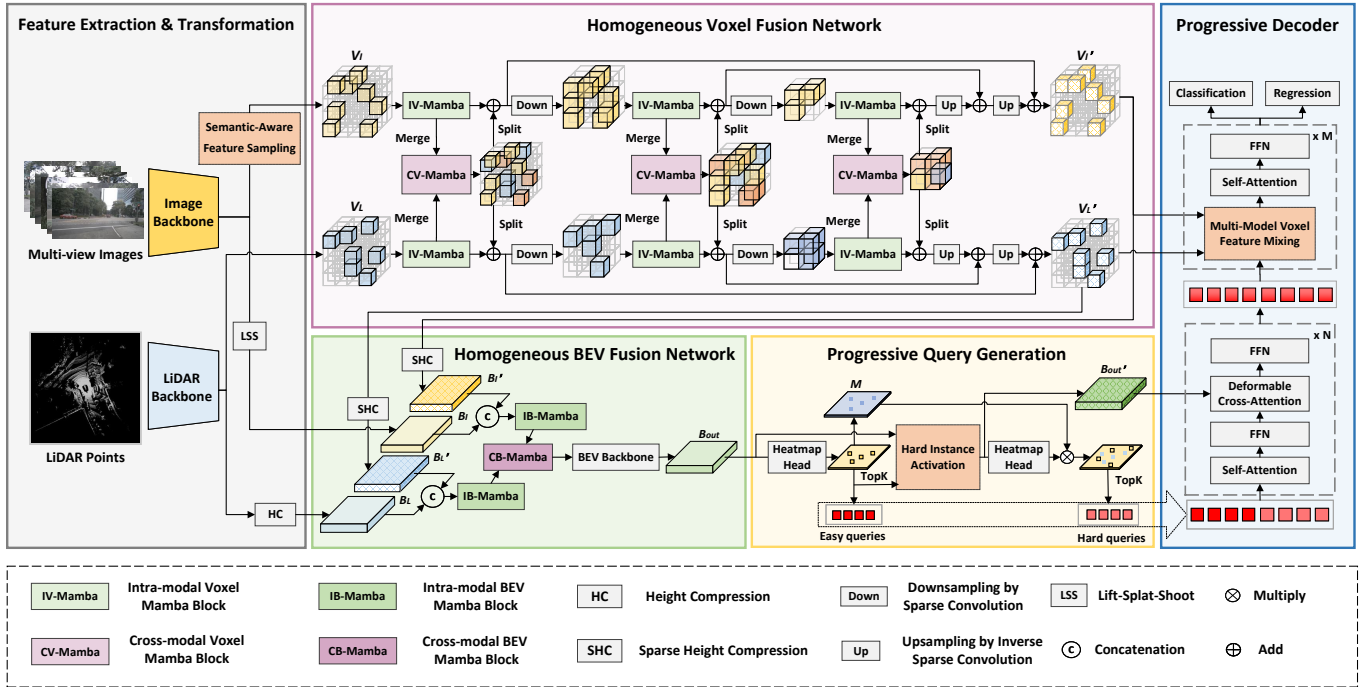


Fig. 2. Overview of DDHFusion. It begins by extracting features from multi-view images and LiDAR point cloud and transforms both into the voxel and BEV domains. These features are then passed to two Mamba-based homogeneous fusion networks, which perform feature alignment and global perception. The resulting high-quality fused BEV feature B_{out} is then fed into the progressive query generation module, which leverages the spatial relationship of easy queries to stimulate the generation of hard queries. Finally, all queries are passed into the progressive decoder, which abstracts dual-domain features around instances for accurate classification and box regression.

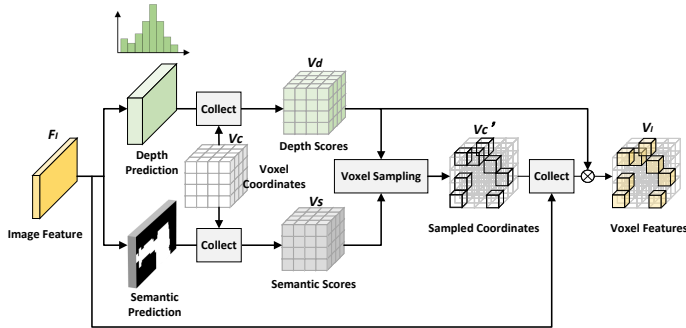


Fig. 3. Details of semantic-aware feature sampling (SAFS). We filter unimportant voxels by depth and semantic scores and transform the image feature to the sparse voxel domain.

B. Homogeneous Voxel Fusion Network

In HVF, we employ a 3D U-Net architecture to fuse LiDAR voxels V_L and image voxels V_I . As illustrated in Fig. 4, the network consists of two parallel branches that process voxel features separately, with feature fusion performed at each scale. Due to the uncertainty of depth estimation and calibration error, V_L and V_I are often misaligned spatially. Previous works [12], [22], [25] only fuse voxel features by concatenation or local gating mechanisms within the same position or a $3 \times 3 \times 3$ neighborhood. However, they fail to resolve the misalignment problem and limit the network’s ability to comprehensively perceive multi-modal information. Inspired by the recent success of Mamba in LiDAR-based 3D

object detection [36], [37], we propose intra-modal and cross-modal voxel Mamba (IV-Mamba and CV-Mamba) modules for feature fusion at each scale. In IV-Mamba, we rearrange the voxels into a 1D sequence based on the 3D Hilbert curve according to [36]. The discrete SSM model is then used to process the entire sequence:

$$\begin{cases} h_i = \bar{A}h_{i-1} + \bar{B}x_i \\ y_{i-1} = \bar{C}h_i + x_i \end{cases} \quad (2)$$

Here, \bar{A} and \bar{B} are derived from the parameters of the continuous SSM using the zero-order hold formula:

$$\begin{cases} \bar{A} = \exp(\Delta A) \\ \bar{B} = (\Delta A)^{-1}(\exp(\Delta A) - I) \bullet \Delta B \end{cases} \quad (3)$$

Where Δ denotes the time-scale parameter and A denotes the learnable matrix. B , C , and Δ are inferred from the input sequence x_i through linear layers, ensuring the input-specific of the SSM model. To ensure complete perception, both forward and backward SSMs are implemented. Their output sequences are added together and modulated by Y to produce the final results.

In CV-Mamba, we directly combine multi-modal voxels in the unified 3D space. It’s important to note that the height range of image voxels Z_I is twice that of LiDAR voxels Z_L . Therefore, we need to multiple the z indices of LiDAR voxels by two before combination. Similar to IV-mamba, these voxels are unfolded into 1D sequences and fed into the SSM. While some voxels may occupy the same position, we treat them as distinct elements in the sequence rather than

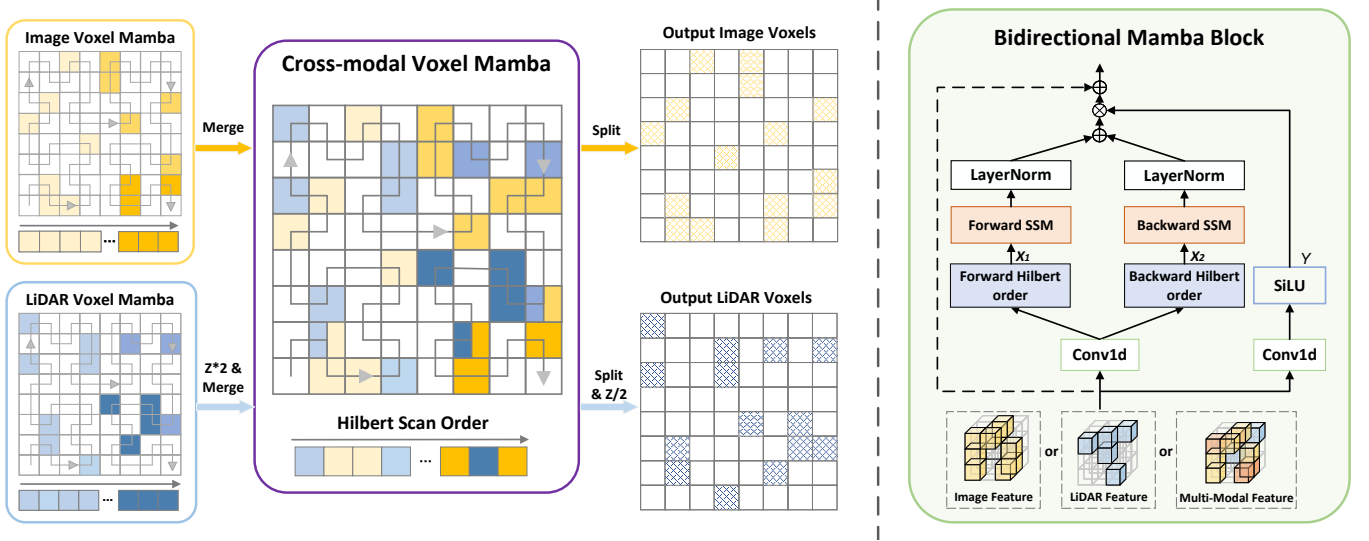


Fig. 4. Pipeline of Mamba-based Voxel Fusion. We utilize the bidirectional Mamba block, as illustrated in the right figure, to process both single-modal and multi-modal voxel features. Within the 3D U-Net architecture, the merge-and-split operation seamlessly switches between intra-modal and cross-modal Mamba blocks, facilitating global alignment and fusion of multi-modal information.

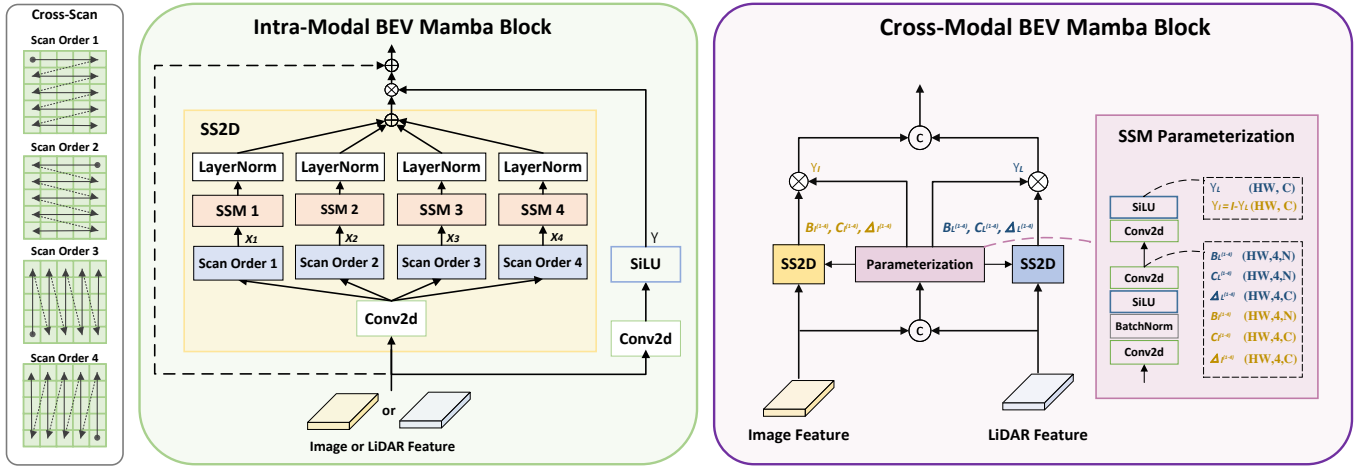


Fig. 5. Details of Intra-Modal and Cross-Modal BEV Mamba. We apply a 4-directional cross-scan to unfold the BEV feature into 1D sequences, which helps construct a more comprehensive spatial relationship. In the cross-modal Mamba block, the parameters for the SSMs of each modality are jointly computed from the Image and LiDAR BEV features, while Z_I and Z_L are used to adaptively modulate the weights of their respective modalities.

merging them as in [25]. According to the theoretical proof in [34], the forward-backward Mamba is a special version of a global transformer, enabling unaligned features to match their corresponding ones in the other modality. Then, the output voxels with different modalities are separated and sent back to their perspective branches, where they are downsampled by sparse 3D convolution. Notably, in most existing works, fusing features with different distributions [22], [23], [25], [42] requires operations such as nearest-neighbor search or grouping, while our designed elegant global merge-and-split operation makes the fusion process more efficient and straightforward. Alternating between IV-Mamba and CV-Mamba effectively bridges the modality gap and alleviates the negative impact of deteriorated data from each modality on the fused features.

Finally, Inverse sparse convolutions are used to upsample voxels features back to the original scale. The output features

V_I and V_L are not directly combined to avoid interfere brought by distinctive voxel distributions. Instead, they are separately fed into the homogeneous BEV fusion network and the multimodal feature mixing module in the decoder.

C. Homogeneous BEV Fusion Network

In Homogeneous BEV Fusion Network, the features from the homogeneous voxel network, V_I' and V_L' , are transformed into BEV grids through sparse height compression [43] — specifically, max-pooling is applied in voxel features belonging to the same BEV pixel, yielding B_I' and B_L' . They are then concatenated with B_I and B_L to inject more 3D semantic and structure details into BEV space. It is important to note that during SAFS, some potential foreground voxels may be filtered out due to low semantic or depth scores. The LSS compensates for this by retaining image information of the

entire environment. In addition, both SAFS and LSS share the same depth map. Since LSS has not undergone feature filtering, it preserves all the backpropagated gradients, which helps accelerate the convergence of depth estimation during training.

As shown in Fig. 4, we also applied the Mamba-based fusion paradigm, which includes both intra-modal and cross-modal BEV Mamba (IB-Mamba and CB-Mamba) modules to generate high-quality BEV features. First the concatenated features into the IB-Mamba, enabling the network to globally perceive modality-specific information. Following the SS2D block proposed in [34], we apply four-directional cross scanning to unfold the image, which helps construct a comprehensive spatial relationship. Then, as described in Equations 2 and 3, the SSM is performed simultaneously across all four directions. After passing through LayerNorm, the outputs are summed and modulated by Y for final results.

In CB-Mamba, to further align multi-modal features in the dense BEV space and adaptively fuse them, we extend the SS2D operation originally designed for single-modal tasks to cross-modal fusion. As shown in Fig. 4, the parameters for the SSM computation are generated from the concatenated tensor, guiding the global rectification for both image and LiDAR features. We describe the SSM parameterization using the following formulas.

$$T = \text{Conv2d}(\text{SiLU}(\text{BatchNorm}(\text{Conv2d}(F_{\text{comb}})))) \quad (4)$$

$$[B_I^{1-4}, C_I^{1-4}, \Delta_I^{1-4}, B_L^{1-4}, C_L^{1-4}, \Delta_L^{1-4}] = \text{Split}(T) \quad (5)$$

Where, the superscripts 1–4 denote the parameters employed for the four-directional scanning in SS2D. Furthermore, the modulation parameters Y_I and Y_L are also generated by concatenating features and are used to reweight multi-modal features:

$$Y_I = \text{SiLU}(\text{Conv2d}(T)) \quad (6)$$

$$Y_L = I - Y_I \quad (7)$$

It enables the network to autonomously favor the more reliable modality, thereby improves adaptability in complex scenarios.

After CB-Mamba, the output BEV tensor is fed into the BEV backbone for further feature propagation, yielding B_{out} , which is then utilized as the input for query generation.

D. Progressive Query Generation

In DDHFusion, the BEV branch is used for efficient generation of target candidates. While many previous works have attempted to achieve this in the range view [44], [45] or sparse 3D space [46], [47], the former is impacted by object occlusions, and the latter often relies on center-voting strategies, which are sensitive to uneven voxel or point densities. In contrast generating queries in the BEV domain is relatively simple. First, we generate a heatmap from B'_{out} with convolution. As outlined in [14], queries can be obtained by processing response scores using non-maximum suppression based on 3x3 max pooling, followed by the top-k selection. However, some hard targets, characterized by corrupted information such as

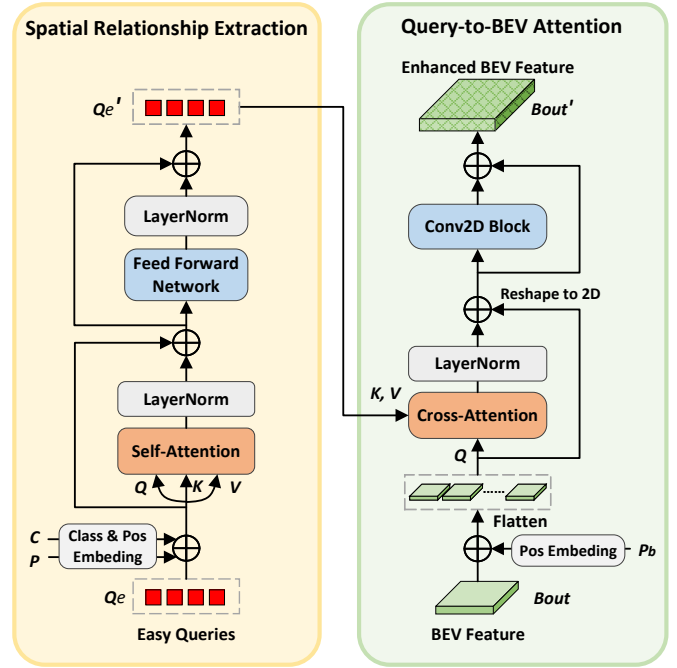


Fig. 6. Details of Hard Instance Activation. First, self-attention among easy queries is used to extract spatial relationships between objects. Then, query-to-BEV attention is applied to activate latent hard instances within the BEV features.

sparse surface points or blurred image textures. After height compression, these features may be further deteriorated. Moreover, since targets are typically small in the BEV plane, their features may be overshadowed during convolution operations in the BEV backbone.

To address this, [48] propose a multi-stage query generation strategy. It groups queries into different difficulty levels and employs residual blocks to activate BEV features between levels to focus on harder instances. In this work, we simplify the approach by dividing queries into two groups: easy queries Q_e and hard queries Q_h . The corresponding two-stage extraction process is detailed in following equations:

$$H_e = \text{Heatmaphead}(B_{\text{out}}) \quad (8)$$

$$Q_e = \text{Topk}(\text{NMS}(B_{\text{out}})) \quad (9)$$

$$M = I - \text{Maxpooling}(H) \quad (10)$$

$$H' = \text{Heatmaphead}(\text{Resnet}(B_{\text{out}})) \quad (11)$$

$$Q_h = \text{Topk}(\text{NMS}(M \bullet H')) \quad (12)$$

Where M represents the mask generated from Q_e , which is used to obtain Q_h by masking the regions corresponding to Q_e . When training, we compute the heatmap loss of the second stage only within the regions of M , guiding the network to focus on hard targets. However, activating BEV feature by the residual block has limited effectiveness—it can only aggregate local information from difficult regions to enhance responses. In the driving environment, the spatial relationships between objects exhibit certain regularities, such as the placement of vehicles and barriers. Based on this observation, we propose a

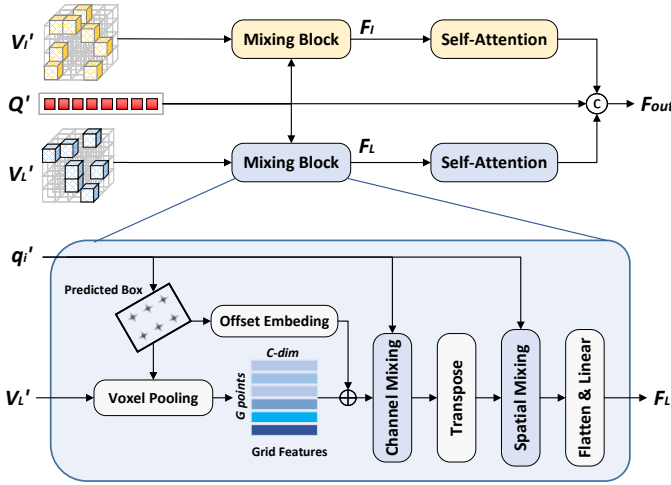


Fig. 7. In the mixing block, queries are used to dynamically aggregate nearby voxel features from each modality. Subsequently, self-attention is employed to aggregate long-range voxel features among instances.

hard instance activation (HIA) module, which leverages easy queries Q_e to activate features in difficult regions. Specifically, we modify Equation 11 as follows:

$$H' = \text{Heatmaphead}(\text{HIA}(Q_e, B_{out})) \quad (13)$$

As shown in Fig 6, in HIA, we first embed categories – in form of one-hot vectors – and positions into the easy queries. Then, we utilize self-attention to extract relationships between objects, resulting in enhanced queries Q'_e . Then, B_{out} is flattened and regarded as query and Q'_e serves as key and value. The query-to-BEV attention [49], [50] is utilized to propagate object relationships to every pixel in the BEV map. Subsequently, the results are reshaped back into a 2D tensor and passed through a residual block to obtain the refined BEV features B'_{out} . Finally, the easy and hard queries along with B'_{out} are fed into the progressive decoder .

E. Progressive Decoder

Many works [7], [9], [48], [50] only decode the BEV features at the end of their models. Although these features are rich in contextual and high-level semantic information, they lack fine-grained geometry-aware details, which limits the accuracy of box regression. To solve this, our progressive decoder (PQ) incorporates features from both BEV and voxel domains .

As shown in Fig 2, we decode the BEV features with several deformable attention blocks to obtain the refined queries q' . They are then fed into the (MMVFM) module to decode voxel features V'_I and V'_L . As depicted in Fig 7, two separate mixing modules are designed to dynamically aggregate voxel features. In each, we first use several linear layers to regress the proposal box b_i from the query q'_i . Then, we divide the box into $G = g \times g \times g$ evenly spaced grid points g_1, \dots, g_G . Next, we extract grid features $Fg = [f_{g1}, \dots, f_{gG}]$ from V_L or V_I using voxel pooling. We then embed offsets $\Delta g_{xk}, \Delta g_{yk}, \Delta g_{zk}$ of each grid point relative to the center of

b_i into F_g through a linear layer, generating shape-aware grid features $F'_g \in \mathbb{R}^{G \times C}$. Following the Adamixer [51] operation, we sequentially perform channel mixing and spatial mixing on them, respectively:

$$C_i = \text{Linear}(q_i) \quad (14)$$

$$F'_g = C_i \times F'_g \quad (15)$$

$$S_i = \text{Linear}(q_i) \quad (16)$$

$$F'_g = S_i \times \text{transpose}(F'_g) \quad (17)$$

Here, $C_i \in \mathbb{R}^{C \times C}$ and $S_i \in \mathbb{R}^{G \times G/4}$ represent the channel and spatial kernels, respectively. After the mixing operation, F'_g is flattened into a vector and passed through a linear layer to reduce the dimensionality to the final output F_I or F_L . It is worth noting that S_i differs in input and output channels from the original design of the adamixer $\mathbb{R}^{G \times G}$, which can reduce the number of parameters by compressing the spatial dimension. Following the aforementioned local mixing operation, we further aggregate long-range 3D features between objects with self-attention mechanisms. Finally, the features from both modalities, along with queries, are concatenated as the output. Subsequently, we decode the fused features through self-attention and a feed-forward layer. Finally, confidences and bounding boxes are regressed by a detection head.

IV. EXPERIMENT

Our method is evaluated on the challenging NuScenes dataset. In this section, we first describe the dataset and implementation details, then report the evaluation performance of DDHFusion. Furthermore, we conduct ablation studies and comparison experiments with other homogeneous fusion methods for a thorough analysis.

A. Experimental Setup

Dataset. The nuScenes dataset is notable for its multi-sensor setup, which includes LiDAR, camera, radar, and GPS/IMU data, enabling comprehensive multi-modal research. It comprises 1,000 diverse driving scenarios, with a standardized split of 700 scenes for training, 150 for validation, and 150 for testing. It also features 10 object categories, such as cars, pedestrians, and cyclists, with over 1.4 million 3D bounding boxes annotated across various driving conditions. For 3D object detection, two key metrics are employed: mean Average Precision (mAP) and the nuScenes Detection Score (NDS), which collectively provide a holistic assessment of model performance. The mAP is computed by averaging the precision across 10 categories at distance thresholds of 0.5m, 1m, 2m, and 4m. NDS, on the other hand, is a composite metric that combines mAP with five True Positive (TP) error measures: mean Average Translation Error (mATE), mean Average Scale Error (mASE), mean Average Orientation Error (mAOE), mean Average Velocity Error (mAVE), and mean Average Attribute Error (mAAE).

Implementation Details. Our model is implemented on the MMDetection3D framework. For the LiDAR backbone, we employ VoxelNet [52], while Swin-T serves as the image

TABLE III
ABLATION STUDY OF EACH MODULE.

Methods	HVF	HBF	PQG	PD	mAP	NDS
(1)					68.4	71.2
(2)	✓				70.0	72.1
(3)		✓			69.1	71.8
(4)	✓	✓			70.6	72.6
(5)	✓	✓	✓		71.4	73.1
(6)	✓	✓	✓	✓	71.6	73.8

TABLE IV
ABLATION STUDY OF HVF.

Methods	IV-Mamba	CV-Mamba	mAP	NDS
(1)			68.2	71.2
(2)	✓		69.4	71.9
(3)		✓	69.6	71.8
(4)	✓	✓	70.0	72.3

TABLE V
ABLATION STUDY OF DIFFERENT DOWNSAMPLING STRIDES IN HVF.

Method	Voxel Stride	mAP	NDS
(1)	[1]	69.6	71.9
(2)	[1, 2]	69.8	72.2
(3)	[1, 2, 4]	70.0	72.3

TABLE VI
ABLATION STUDY OF HBF.

Methods	IB-Mamba	CB-Mamba	mAP	NDS
(1)			70.0	72.3
(2)	✓		70.3	72.4
(3)		✓	70.5	72.5
(4)	✓	✓	70.8	72.7

C. Ablation Studies

In this section, we demonstrate the effectiveness of each component through comprehensive ablation studies.

Ablation of each module As shown in Table V, we evaluate the contribution of each module to the detection performance. We replace the decoder in BEVFusion with deformable attention as the baseline. First, the proposed voxel fusion network significantly improves performance by 1.6 mAP and 0.9 NDS. Introducing only the BEV fusion network also provides a gain of 0.7 mAP and 0.5 NDS. As reported in the third row, the combination of both homogeneous fusion networks achieves a substantial improvement of 2.2 mAP and 1.4 NDS. Additionally, the progressive query generation module enhances object detection recall, contributing 0.7 mAP. Finally, integrating voxel decoder into the original BEV decoder to form the progressive decoder further increases performance by 0.3 mAP and 0.7 NDS. In summary, the four proposed components fully exploit the potential of dual-domain multi-modal features for high-performance object detection.

TABLE VII
COMPARISON OF DIFFERENT ACTIVATION METHODS IN PQG.

Activation Methods	mAP	NDS
baseline	70.8	72.7
ResNet [48]	71.0	72.8
HIA (ours)	71.4	73.0

TABLE VIII
COMPARISON OF DIFFERENT DECODER NUMBERS IN MMVFM.

Methods	BEV decoder N	voxel decoder M	mAP	NDS
(1)	0	1	70.9	72.6
(2)	3	0	71.4	73.1
(3)	3	1	71.6	73.8
(4)	3	2	71.5	73.9
(5)	3	3	71.6	73.7

TABLE IX
ABLATION STUDY OF MMVFM

Methods	mixing block	self-attention	mAP	NDS
(1)			71.4	73.0
(2)	✓		71.5	73.3
(3)		✓	71.6	73.4
(4)	✓	✓	71.6	73.8

TABLE X
COMPARISON OF IMAGE SIZES AND CHANNELS OF LiDAR BACKBONE.

Model	Image Size or Channels	mAP	NDS
Image Backbone	256×704	–	–
	384×1056	–	–
LiDAR Backbone	(16,32,64,128)	–	–
	(32,64,128,256)	–	–

Analysis of homogeneous voxel fusion network As shown in Table IV, we analyze the role of the Mamba-based modules in the voxel fusion stage. In the second row, we introduce a 3D U-Net with only IV-Mamba, without directly fusing image and LiDAR voxels. This approach improves performance by 1.2 mAP and 0.5 NDS, demonstrating that IV-Mamba can effectively capture long-range dependencies within each modality. The CV-Mamba can also enhance network performance, indicating the effectiveness of global fusion of voxels with different modalities and distributions. By combining both approaches with a simple merge-and-split strategy, we not only align multi-modal features but also preserve the relative independence of each modality, avoiding interference from noise or low-quality information from other modality, thereby further improving accuracy. As shown in Table V, setting the voxel strides to [1, 2, 4] in HVF achieves the best performance, as increasing the downsampling rate allows the network to capture structural information at different granularities.

Analysis of homogeneous BEV fusion network We further investigate HBF. As shown in Table VI, the SS2D module in the IB-Mamba enables full-scene feature propagation across the dense BEV map in four directions, resulting in improvements of 0.3 mAP and 0.1 NDS. Our proposed CB-Mamba

achieves gains of 0.5 mAP and 0.2 NDS. It effectively propagates multi-modal features while adaptively exploring their latent relationships, thereby eliminating feature misalignment in the BEV domain. Notably, the combination of IB-Mamba and CB-Mamba yields the best performance, which benefits subsequent the query generation and decoder process.

Comparison of different activation method In PQG, we explore different methods to activate BEV features for extracting harder queries in the second stage. As shown in Table VII, following the approach described in [48], utilizing a residual block yields a minor improvement of 0.2 mAP and 0.1 NDS. Our proposed HIA module further incorporates spatial cues from easy queries, enabling the identification of remaining hard objects in driving scenarios and achieving higher accuracy gains. However, it is important to note that the cross-attention between queries and BEV features introduces additional computational overhead, which limits the number of queries and stages. We plan to address this issue in the future work.

Analysis of progressive decoder In the progressive decoder, both BEV-based and voxel-based decoders are employed for query refinement. As shown in Table IX, we explore various configurations of their layer counts (M and N) to analyze their impact on performance. In the first row, using only a single voxel-based decoder yields suboptimal accuracy, even underperforming the second row, which adopts a 3-layer BEV decoder as in [48]. The BEV map at the end of the network contains richer contextual information and higher-level semantic features compared to voxels. Additionally, its dense representation is more robust to point cloud density variations than sparse voxel representation, both of which are critical for object detection in complex environments. However, as shown in the third row, adding a voxel decoder after the BEV decoder improves performance by 0.2 mAP and 0.7 NDS, indicating that incorporating voxel features with fine geometric details can enhance regression accuracy of predicted boxes. However, further increasing layer counts provides negligible performance gains. In Table X, we demonstrate that the mixing block and self-attention mechanism can adaptively aggregate shape features and long-range spatial information respectively, each contributing to performance improvements. As reported in the last row, combining them achieves the best results.

Analysis of on different scaling choices

D. Comparison of Different Homogeneous Fusion Methods

We further compare DDHFusion with other three representative homogeneous fusion methods mentioned in the introduction, including GraphBEV, DeepInteraction++, and UVTR, through extensive experiments.

First, we evaluate their performance under different weather and lighting conditions. Since DeepInteraction++ and UVTR do not provide relevant data in their papers, we reproduce

TABLE XI
PERFORMANCE COMPARISONS UNDER DIFFERENT LIGHTING AND WEATHER CONDITIONS

Method	Sunny	Rainy	Day	Night
GraphBEV [9]	70.1	70.2	69.7	45.1
Deepinteraction++ [60]	70.3	70.4	70.6	42.9
UVTR [12]	66.4	65.1	65.5	36.7
DDHFusion (ours)	71.8	71.9	71.8	46.8

TABLE XII
PERFORMANCE COMPARISONS WITH DIFFERENT EGO DISTANCES

Method	Near	Middle	Far
GraphBEV [9]	78.6	65.3	42.1
Deepinteraction++ [60]	80.0	66.5	42.4
UVTR [12]	77.2	61.2	37.0
DDHFusion (ours)	82.3	67.8	44.2

their models using open-source code to obtain the accuracy. As shown in Table XI, DDHFusion achieves the highest mAP across all environments. Unlike UVTR, DDHFusion is not negatively affected by rainy conditions and performs better even in poor lighting environments. This robustness stems from the comprehensive intra-modal and cross-modal feature learning in DDHFusion, which progressively filters out corrupt information to learn robust latent representations. Additionally, as shown in Table XII, we evaluate the performance of different models on object detection at varying distances, where “Near,” “Middle,” and “Far” represent ranges of $< 20\text{m}$, $[20\text{m}, 30\text{m}]$, and $> 30\text{m}$, respectively. Again, our proposed DDHFusion outperforms other methods across all distance ranges.

Figure 8 showcases the detection results of DDHFusion, demonstrating its ability to accurately classify and localize objects of various categories in complex environments. Figure 9 provides a qualitative comparison with other models. As shown in the first row, DDHFusion successfully detects three distant and crowded objects. In the second row, bounding boxes generated by DDHFusion show minimal deviations. In the third row, it successfully identifies the small and distant object that other methods fail to detect. These results highlight the superiority of our dual-domain homogeneous fusion approach.

Our method demonstrates competitive performance in terms of both memory consumption and runtime, highlighting its efficiency and practicality. For a fair comparison, all models are deployed in the mmdetection framework and tested on a single 4090D GPU. As shown in Table XIII, The computational resource consumption of DDHFusion is affordable,

TABLE XIII
COMPARISON OF MEMORY COST AND INFERENCE SPEED.

Method	Memory (MB)	FPS
GraphBEV [9]	9851	5.7
Deepinteraction++ [60]	13125	3.8
UVTR [12]	17640	3.6
DDHFusion (ours)	12189	4.2



Fig. 8. The visualization of DDHFusion on nuScenes validation set.

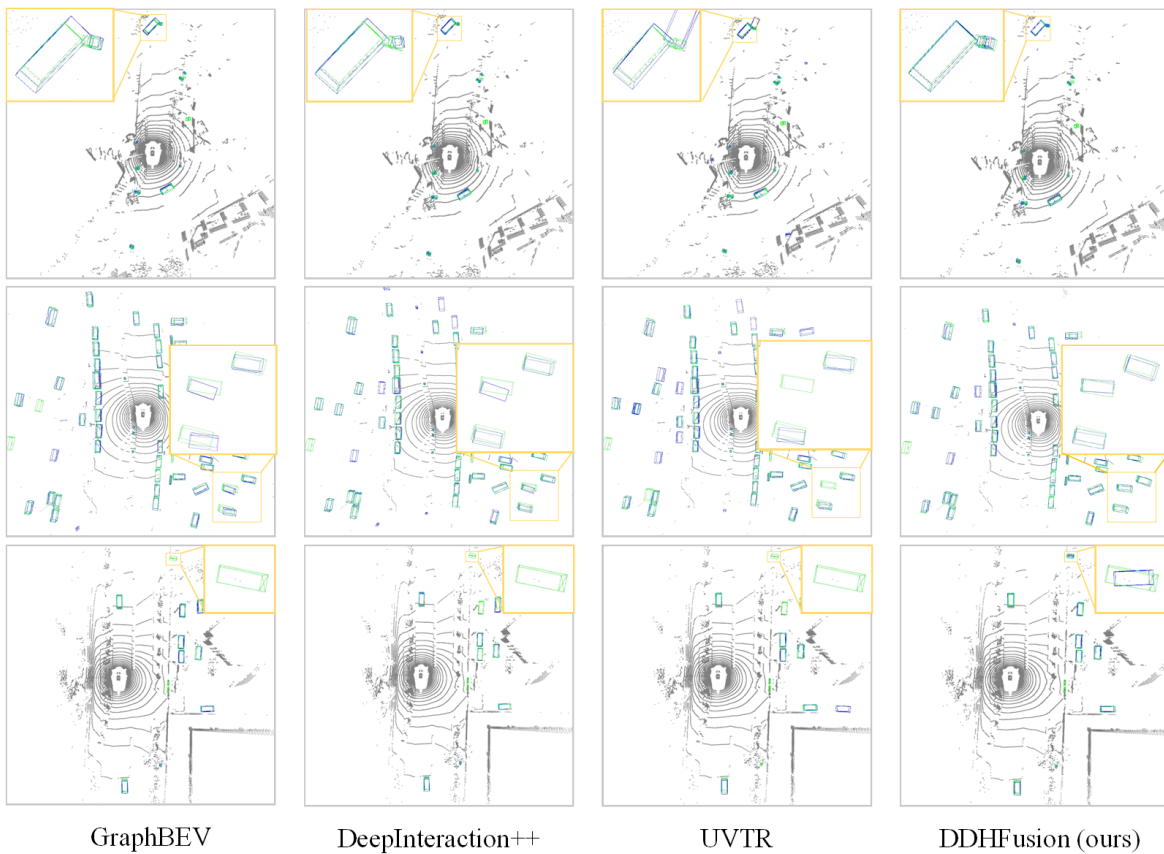


Fig. 9. The visualization of different methods on nuScenes validation set. The green and blue boxes represent ground truths and inference results respectively

demonstrating the efficiency of our Mamba-based fusion modules. GraphBEV is the most lightweight, as it performs fusion only in the BEV domain. In contrast, UVTR incurs the highest computational burden due to its retention of dense voxels, while DDHFusion mitigates this issue through voxel sampling operations. Notably, DeepInteraction++ employs flash-attention for acceleration. Similarly, we believe that further hardware optimization of Mamba could significantly improve efficiency.

V. CONCLUSION

REFERENCES

- [1] S. Vora, A. H. Lang, B. Helou, and O. Beijbom, "PointPainting: Sequential Fusion for 3D Object Detection," *2020 IEEE/CVF Conference on Computer Vision and Pattern Recognition (CVPR)*, pp. 4603–4611, Jun. 2020, conference Name: 2020 IEEE/CVF Conference on Computer Vision and Pattern Recognition (CVPR) ISBN: 9781728171685 Place: Seattle, WA, USA Publisher: IEEE. [Online]. Available: <https://ieeexplore.ieee.org/document/9156790/>
- [2] L. Zhao, M. Wang, and Y. Yue, "Sem-Aug: Improving Camera-LiDAR Feature Fusion With Semantic Augmentation for 3D Vehicle Detection," *IEEE Robotics and Automation Letters*, vol. 7, no. 4, pp. 9358–9365, Oct. 2022. [Online]. Available: <https://ieeexplore.ieee.org/document/9830844/>
- [3] M. Wang, L. Zhao, and Y. Yue, "PA3DNet: 3-D Vehicle Detection With Pseudo Shape Segmentation and Adaptive Camera-LiDAR Fusion," *IEEE Transactions on Industrial Informatics*, vol. 19, no. 11, pp. 10 693–10 703, Nov. 2023, conference Name: IEEE Transactions on Industrial Informatics. [Online]. Available: <https://ieeexplore.ieee.org/document/10034840/>
- [4] S. Xu, D. Zhou, J. Fang, J. Yin, Z. Bin, and L. Zhang, "FusionPainting: Multimodal Fusion with Adaptive Attention for 3D Object Detection," *2021 IEEE International Intelligent Transportation Systems Conference (ITSC)*, pp. 3047–3054, Sep. 2021, conference Name: 2021 IEEE International Intelligent Transportation Systems Conference (ITSC) ISBN: 9781728191423 Place: Indianapolis, IN, USA Publisher: IEEE. [Online]. Available: <https://ieeexplore.ieee.org/document/9564951/>
- [5] "Improving data augmentation for multi-modality 3d object detection," 2021. [Online]. Available: <https://api.semanticscholar.org/CorpusID:237311015>
- [6] Y. Yang, H. Yin, A. Chong, J. Wan, and Q.-Y. Liu, "Sacinet: Semantic-aware cross-modal interaction network for real-time 3d object detection," *IEEE Transactions on Intelligent Vehicles*, vol. 9, pp. 3917–3927, 2024. [Online]. Available: <https://api.semanticscholar.org/CorpusID:266661772>
- [7] Z. Liu, H. Tang, A. Amini, X. Yang, H. Mao, D. L. Rus, and S. Han, "BEVFusion: Multi-Task Multi-Sensor Fusion with Unified Bird's-Eye View Representation," *2023 IEEE International Conference on Robotics and Automation (ICRA)*, pp. 2774–2781, May 2023, conference Name: 2023 IEEE International Conference on Robotics and Automation (ICRA) ISBN: 9798350323658 Place: London, United Kingdom Publisher: IEEE. [Online]. Available: <https://ieeexplore.ieee.org/document/10160968/>
- [8] T. Liang, H. Xie, K. Yu, Z. Xia, Z. Lin, Y. Wang, T. Tang, B. Wang, and Z. Tang, "BEVFusion: A Simple and Robust LiDAR-Camera Fusion Framework," 2022, publisher: arXiv Version Number: 3. [Online]. Available: <https://arxiv.org/abs/2205.13790>
- [9] Z. Song, L. Yang, S. Xu, L. Liu, D. Xu, C. Jia, F. Jia, and L. Wang, "Graphbev: Towards robust bev feature alignment for multi-modal 3d object detection," *ArXiv*, vol. abs/2403.11848, 2024. [Online]. Available: <https://api.semanticscholar.org/CorpusID:268532341>
- [10] Z. Yang, J.-Q. Chen, Z. Miao, W. Li, X. Zhu, and L. Zhang, "Deepinteraction: 3d object detection via modality interaction," *ArXiv*, vol. abs/2208.11112, 2022. [Online]. Available: <https://api.semanticscholar.org/CorpusID:251741547>
- [11] Z. Yang, N. Song, W. Li, X. Zhu, L. Zhang, and P. H. S. Torr, "DeepInteraction++: Multi-Modality Interaction for Autonomous Driving," Aug. 2024, arXiv:2408.05075 [cs]. [Online]. Available: <http://arxiv.org/abs/2408.05075>
- [12] Y. Li, Y. Chen, X. Qi, Z. Li, J. Sun, and J. Jia, "Unifying voxel-based representation with transformer for 3d object detection," *ArXiv*, vol. abs/2206.00630, 2022. [Online]. Available: <https://api.semanticscholar.org/CorpusID:249240467>
- [13] S. Deng, Z. Liang, L. Sun, and K. Jia, "Vista: Boosting 3d object detection via dual cross-view spatial attention," *2022 IEEE/CVF Conference on Computer Vision and Pattern Recognition (CVPR)*, pp. 8438–8447, 2022. [Online]. Available: <https://api.semanticscholar.org/CorpusID:247594044>
- [14] X. Bai, Z. Hu, X. Zhu, Q. Huang, Y. Chen, H. Fu, and C.-L. Tai, "Transfusion: Robust lidar-camera fusion for 3d object detection with transformers," *2022 IEEE/CVF Conference on Computer Vision and Pattern Recognition (CVPR)*, pp. 1080–1089, 2022. [Online]. Available: <https://api.semanticscholar.org/CorpusID:247597200>
- [15] J. H. Yoo, Y. Kim, J. S. Kim, and J. W. Choi, "3d-cvf: Generating joint camera and lidar features using cross-view spatial feature fusion for 3d object detection," in *European Conference on Computer Vision*, 2020. [Online]. Available: <https://api.semanticscholar.org/CorpusID:216552886>
- [16] B. Tao, F. Yan, Z. Yin, L. Nie, M. Miao, Y. Jiao, and C. Lei, "A Multimodal 3-D Detector With Attention From the Corresponding Modal," *IEEE Sensors Journal*, vol. 23, no. 8, pp. 8581–8590, Apr. 2023, conference Name: IEEE Sensors Journal. [Online]. Available: <https://ieeexplore.ieee.org/document/10064270>
- [17] J. Huang, G. Huang, Z. Zhu, and D. Du, "Bevdet: High-performance multi-camera 3d object detection in bird-eye-view," *ArXiv*, vol. abs/2112.11790, 2021. [Online]. Available: <https://api.semanticscholar.org/CorpusID:245385398>
- [18] Z. Song, F. Jia, H. Pan, Y. Luo, C. Jia, G. Zhang, L. Liu, Y. Ji, L. Yang, and L. Wang, "Contrastalign: Toward robust bev feature alignment via contrastive learning for multi-modal 3d object detection," *ArXiv*, vol. abs/2405.16873, 2024. [Online]. Available: <https://api.semanticscholar.org/CorpusID:270062922>
- [19] J. Fu, C. Gao, Z. Wang, L. Yang, X. Wang, B. Mu, and S. Liu, "Eliminating cross-modal conflicts in bev space for lidar-camera 3d object detection," *2024 IEEE International Conference on Robotics and Automation (ICRA)*, pp. 16 381–16 387, 2024. [Online]. Available: <https://api.semanticscholar.org/CorpusID:268363442>
- [20] J. Wang, F. Li, Y. An, X. Zhang, and H. Sun, "Toward robust lidar-camera fusion in bev space via mutual deformable attention and temporal aggregation," *IEEE Transactions on Circuits and Systems for Video Technology*, vol. 34, pp. 5753–5764, 2024. [Online]. Available: <https://api.semanticscholar.org/CorpusID:267736772>
- [21] H. Hu, F. Wang, J. Su, Y. Wang, L. Hu, W. Fang, J. Xu, and Z. Zhang, "Ea-Iss: Edge-aware lift-splat-shot framework for 3d bev object detection," 2023. [Online]. Available: <https://api.semanticscholar.org/CorpusID:257900888>
- [22] H. Li, T. Ge, K. Bai, G. Nie, L. Xu, X. Ai, and S. Cao, "Multimodal 3d object detection based on sparse interaction in internet of vehicles," *IEEE Transactions on Vehicular Technology*, vol. 74, pp. 2174–2186, 2025. [Online]. Available: <https://api.semanticscholar.org/CorpusID:267215837>
- [23] X. Wu, L. Peng, H. Yang, L. Xie, C. Huang, C. Deng, H. Liu, and D. Cai, "Sparse fuse dense: Towards high quality 3d detection with depth completion," *2022 IEEE/CVF Conference on Computer Vision and Pattern Recognition (CVPR)*, pp. 5408–5417, 2022. [Online]. Available: <https://api.semanticscholar.org/CorpusID:247595289>
- [24] T. Yin, X. Zhou, and P. Krähenbühl, "Multimodal virtual point 3d detection," *ArXiv*, vol. abs/2111.06881, 2021. [Online]. Available: <https://api.semanticscholar.org/CorpusID:244102957>
- [25] Y. Jiao, Z. Jie, S. Chen, J. Chen, X. Wei, L. Ma, and Y.-G. Jiang, "Msmdfusion: Fusing lidar and camera at multiple scales with multi-depth seeds for 3d object detection," *2023 IEEE/CVF Conference on Computer Vision and Pattern Recognition (CVPR)*, pp. 21 643–21 652, 2022. [Online]. Available: <https://api.semanticscholar.org/CorpusID:252111042>
- [26] J. Ahmad and A. D. Bue, "mmfusion: Multimodal fusion for 3d objects detection," *ArXiv*, vol. abs/2311.04058, 2023. [Online]. Available: <https://api.semanticscholar.org/CorpusID:265043073>
- [27] Y. Song and L. Wang, "Bico-fusion: Bidirectional complementary lidar-camera fusion for semantic- and spatial-aware 3d object detection," *IEEE Robotics and Automation Letters*, vol. 10, pp. 1457–1464,

2024. [Online]. Available: <https://api.semanticscholar.org/CorpusID:270764622>
- [28] A. Gu, K. Goel, and C. R'e, "Efficiently modeling long sequences with structured state spaces," *ArXiv*, vol. abs/2111.00396, 2021. [Online]. Available: <https://api.semanticscholar.org/CorpusID:240354066>
- [29] A. Gupta and J. Berant, "Diagonal state spaces are as effective as structured state spaces," *ArXiv*, vol. abs/2203.14343, 2022. [Online]. Available: <https://api.semanticscholar.org/CorpusID:247762199>
- [30] A. Gu, I. Johnson, K. Goel, K. K. Saab, T. Dao, A. Rudra, and C. R'e, "Combining recurrent, convolutional, and continuous-time models with linear state-space layers," in *Neural Information Processing Systems*, 2021. [Online]. Available: <https://api.semanticscholar.org/CorpusID:239998472>
- [31] A. Gu, T. Dao, S. Ermon, A. Rudra, and C. Ré, "Hippo: Recurrent memory with optimal polynomial projections," *ArXiv*, vol. abs/2008.07669, 2020. [Online]. Available: <https://api.semanticscholar.org/CorpusID:221150566>
- [32] A. Gu and T. Dao, "Mamba: Linear-time sequence modeling with selective state spaces," *ArXiv*, vol. abs/2312.00752, 2023. [Online]. Available: <https://api.semanticscholar.org/CorpusID:265551773>
- [33] L. Zhu, B. Liao, Q. Zhang, X. Wang, W. Liu, and X. Wang, "Vision mamba: Efficient visual representation learning with bidirectional state space model," *ArXiv*, vol. abs/2401.09417, 2024. [Online]. Available: <https://api.semanticscholar.org/CorpusID:267028142>
- [34] Y. Liu, Y. Tian, Y. Zhao, H. Yu, L. Xie, Y. Wang, Q. Ye, and Y. Liu, "Vmamba: Visual state space model," *ArXiv*, vol. abs/2401.10166, 2024. [Online]. Available: <https://api.semanticscholar.org/CorpusID:267035250>
- [35] D. Liang, X. Zhou, W. Xu, X. Zhu, Z. Zou, X. Ye, X. Tan, and X. Bai, "Pointmamba: A simple state space model for point cloud analysis," *ArXiv*, vol. abs/2402.10739, 2024. [Online]. Available: <https://api.semanticscholar.org/CorpusID:267740688>
- [36] G. Zhang, L. Fan, C. He, Z. Lei, Z. Zhang, and L. Zhang, "Voxel mamba: Group-free state space models for point cloud based 3d object detection," *ArXiv*, vol. abs/2406.10700, 2024. [Online]. Available: <https://api.semanticscholar.org/CorpusID:270559452>
- [37] Z. Liu, J. Hou, X. Wang, X. Ye, J. Wang, H. Zhao, and X. Bai, "Lion: Linear group rnn for 3d object detection in point clouds," *ArXiv*, vol. abs/2407.18232, 2024. [Online]. Available: <https://api.semanticscholar.org/CorpusID:271431965>
- [38] Z. You, H. Wang, Q. Zhao, and J. Wang, "Mambabev: An efficient 3d detection model with mamba2," *ArXiv*, vol. abs/2410.12673, 2024. [Online]. Available: <https://api.semanticscholar.org/CorpusID:273375095>
- [39] Y. Tian, S. Bai, Z. Luo, Y. Wang, Y. Lv, and F.-Y. Wang, "Mambaocc: Visual state space model for bev-based occupancy prediction with local adaptive reordering," *ArXiv*, vol. abs/2408.11464, 2024. [Online]. Available: <https://api.semanticscholar.org/CorpusID:271916087>
- [40] Y. Chen, J. Liu, X. Zhang, X. Qi, and J. Jia, "Voxelnext: Fully sparse voxelnet for 3d object detection and tracking," *2023 IEEE/CVF Conference on Computer Vision and Pattern Recognition (CVPR)*, pp. 21 674–21 683, 2023. [Online]. Available: <https://api.semanticscholar.org/CorpusID:257631740>
- [41] J. Zhang, Y. Zhang, Q. Liu, and Y. Wang, "Sa-bev: Generating semantic-aware bird's-eye-view feature for multi-view 3d object detection," *2023 IEEE/CVF International Conference on Computer Vision (ICCV)*, pp. 3325–3334, 2023. [Online]. Available: <https://api.semanticscholar.org/CorpusID:260091236>
- [42] H. Wang, H. Tang, S. Shi, A. Li, Z. Li, B. Schiele, and L. Wang, "Unitr: A unified and efficient multi-modal transformer for bird's-eye-view representation," *2023 IEEE/CVF International Conference on Computer Vision (ICCV)*, pp. 6769–6779, 2023. [Online]. Available: <https://api.semanticscholar.org/CorpusID:260900346>
- [43] Z. Song, G. Zhang, J. Xie, L. Liu, C. Jia, S. Xu, and Z. Wang, "VoxelNextFusion: A Simple, Unified, and Effective Voxel Fusion Framework for Multimodal 3-D Object Detection," *IEEE Transactions on Geoscience and Remote Sensing*, vol. 61, pp. 1–12, 2023. [Online]. Available: <https://ieeexplore.ieee.org/document/10314564/>
- [44] L. Fan, X. Xiong, F. Wang, N. Wang, and Z. Zhang, "RangeDet: In Defense of Range View for LiDAR-based 3D Object Detection," Mar. 2021, arXiv:2103.10039 [cs]. [Online]. Available: <http://arxiv.org/abs/2103.10039>
- [45] Q. Meng, X. Wang, J. Wang, L. Yan, and K. Wang, "Small, Versatile and Mighty: A Range-View Perception Framework," 2024, publisher: arXiv Version Number: 1. [Online]. Available: <https://arxiv.org/abs/2403.00325>
- [46] Z. Yang, Y. Sun, S. Liu, and J. Jia, "3dssd: Point-based 3d single stage object detector," *2020 IEEE/CVF Conference on Computer Vision and Pattern Recognition (CVPR)*, pp. 11 037–11 045, 2020. [Online]. Available: <https://api.semanticscholar.org/CorpusID:211259226>
- [47] L. Fan, F. Wang, N. Wang, and Z. Zhang, "Fully Sparse 3D Object Detection," 2022, publisher: arXiv Version Number: 2. [Online]. Available: <https://arxiv.org/abs/2207.10035>
- [48] Y. Chen, Z. Yu, Y. Chen, S. Lan, A. Anandkumar, J. Jia, and J. M. Álvarez, "Focalformer3d : Focusing on hard instance for 3d object detection," *2023 IEEE/CVF International Conference on Computer Vision (ICCV)*, pp. 8360–8371, 2023. [Online]. Available: <https://api.semanticscholar.org/CorpusID:260736073>
- [49] Z. Chen, S. Xu, M. Ye, Z. Qian, X. Zou, D.-Y. Yeung, and Q. Chen, "Learning high-resolution vector representation from multi-camera images for 3d object detection," in *European Conference on Computer Vision*, 2024. [Online]. Available: <https://api.semanticscholar.org/CorpusID:271328261>
- [50] J. Yin, J. Shen, R. Chen, W. Li, R. Yang, P. Frossard, and W. Wang, "Is-fusion: Instance-scene collaborative fusion for multimodal 3d object detection," *2024 IEEE/CVF Conference on Computer Vision and Pattern Recognition (CVPR)*, pp. 14 905–14 915, 2024. [Online]. Available: <https://api.semanticscholar.org/CorpusID:268667232>
- [51] Z. Gao, L. Wang, B. Han, and S. Guo, "Adamixer: A fast-converging query-based object detector," *2022 IEEE/CVF Conference on Computer Vision and Pattern Recognition (CVPR)*, pp. 5354–5363, 2022. [Online]. Available: <https://api.semanticscholar.org/CorpusID:247792998>
- [52] Y. Yan, Y. Mao, and B. Li, "Second: Sparsely embedded convolutional detection," *Sensors (Basel, Switzerland)*, vol. 18, 2018. [Online]. Available: <https://api.semanticscholar.org/CorpusID:52957856>
- [53] R. Li, X. Li, P.-A. Heng, and C.-W. Fu, "Pointaugmt: An auto-augmentation framework for point cloud classification," *2020 IEEE/CVF Conference on Computer Vision and Pattern Recognition (CVPR)*, pp. 6377–6386, 2020. [Online]. Available: <https://api.semanticscholar.org/CorpusID:211296277>
- [54] A. H. Lang, S. Vora, H. Caesar, L. Zhou, J. Yang, and O. Beijbom, "Pointpillars: Fast encoders for object detection from point clouds," *2019 IEEE/CVF Conference on Computer Vision and Pattern Recognition (CVPR)*, pp. 12 689–12 697, 2018. [Online]. Available: <https://api.semanticscholar.org/CorpusID:55701967>
- [55] T. Yin, X. Zhou, and P. Krährenbühl, "Center-based 3d object detection and tracking," *2021 IEEE/CVF Conference on Computer Vision and Pattern Recognition (CVPR)*, pp. 11 779–11 788, 2020. [Online]. Available: <https://api.semanticscholar.org/CorpusID:219956621>
- [56] Y. Chen, J. Liu, X. Zhang, X. Qi, and J. Jia, "Largekernel3d: Scaling up kernels in 3d sparse cnns," *2023 IEEE/CVF Conference on Computer Vision and Pattern Recognition (CVPR)*, pp. 13 488–13 498, 2022. [Online]. Available: <https://api.semanticscholar.org/CorpusID:257663653>
- [57] Z. Chen, Z. Li, S. Zhang, L. Fang, Q. Jiang, and F. Zhao, "Autoalignv2: Deformable feature aggregation for dynamic multi-modal 3d object detection," *ArXiv*, vol. abs/2207.10316, 2022. [Online]. Available: <https://api.semanticscholar.org/CorpusID:250919842>
- [58] J. Yan, Y. Liu, J. Sun, F. Jia, S. Li, T. Wang, and X. Zhang, "Cross modal transformer: Towards fast and robust 3d object detection," *2023 IEEE/CVF International Conference on Computer Vision (ICCV)*, pp. 18 222–18 232, 2023. [Online]. Available: <https://api.semanticscholar.org/CorpusID:257496090>
- [59] Q. Cai, Y. Pan, T. Yao, C.-W. Ngo, and T. Mei, "Objectfusion: Multi-modal 3d object detection with object-centric fusion," *2023 IEEE/CVF International Conference on Computer Vision (ICCV)*, pp. 18 021–18 030, 2023. [Online]. Available: <https://api.semanticscholar.org/CorpusID:265255664>
- [60] Z. Yang, N. Song, W. Li, X. Zhu, L. Zhang, and P. H. S. Torr, "Deepinteraction++: Multi-modality interaction for autonomous driving," *ArXiv*, vol. abs/2408.05075, 2024. [Online]. Available: <https://api.semanticscholar.org/CorpusID:271843477>